Size effect in concrete beams: a numerical investigation based on the size effect law

H. S. Vishwanatha
Department of Civil Engineering, M.E.I. Polytechnic; Department of Technical Education, Bangalore, Karnataka, India
hs_vish@yahoo.co.in

S. Muralidhara
Department of Civil Engineering, B.M.S. College of Engineering; Vishveshwarya Technical University, Bangalore, Karnataka, India
murali.civ@bmsce.ac.in

B. K. Raghu Prasad
Department of Civil Engineering, Indian Institute of Science, Bangalore, Karnataka, India
bkriisc@gmail.com

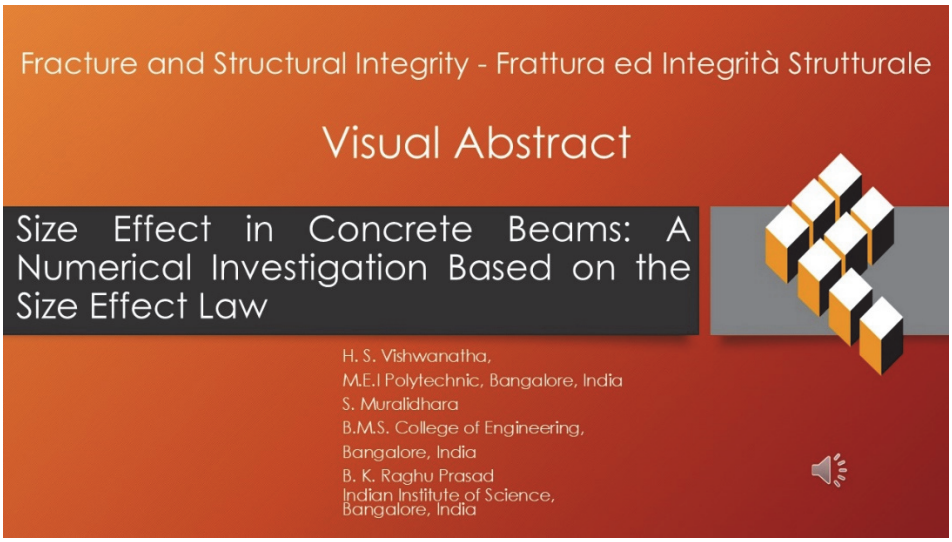

Citation: Vishwanatha, H., Murlidhara, S., Raghu Prasad, B., ISize effect in concrete beams: a numerical investigation based on the size effect law, Fracture and Structural Integrity, 73 (2025) 23-40.

Received: 20.02.2025
Accepted: 06.04.2025
Published: 10.04.2025
Issue: 07.2025

KEYWORDS. Size effect, Fracture Energy, Load-deflection, Interfacial Transition Zone.

INTRODUCTION

Classical strength theories suggest that the strength of geometrically similar structures remains unaffected by size, a concept derived from plasticity analysis. However, concrete, being a quasi-brittle material with a heterogeneous microstructure, deviates from this assumption due to its fracture mechanics-driven failure. The size effect, which

highlights the relationship between structural strength and dimensions, primarily results from energy dissipation linked to crack propagation and stress redistribution.

Bažant's size effect law (BSL) provides a theoretical basis for describing this behavior across various structural scales. Unlike purely plastic or elastic materials, concrete demonstrates a shift from strength-dominated failure in smaller specimens to fracture-dominated failure in larger ones. This transition is largely influenced by the formation of the fracture process zone (FPZ), where microcracks accumulate before a macro-crack fully develops.

During crack initiation, the size effect is governed by stress redistribution, material heterogeneity, and the variability of strength properties. The random distribution of microstructural defects within concrete significantly affects crack formation, making statistical approaches to the size effect essential for understanding failure mechanisms. Recent research has further refined Bažant's model by integrating fracture energy principles and numerical simulations to enhance the understanding of size-dependent fracture behavior in notched concrete beams.

Various theoretical approaches have been introduced to explain the size effect in concrete structures, including statistical, deterministic, and fractal models [1]. Among these, the deterministic approach, which is based on fracture mechanics principles, has been widely studied due to its effectiveness in capturing the failure behavior of quasi-brittle materials like concrete [2,3]. This approach, extensively developed by Bažant, provides a mathematical framework to describe the size-dependent strength reduction observed in concrete elements of varying dimensions.

Bažant's size effect theory, formulated within a deterministic framework, integrates concepts from linear elastic fracture mechanics (LEFM) and cohesive crack models to explain the transition from strength-based to fracture-based failure mechanisms in concrete structures. Unlike conventional plasticity-based models, which assume size-independent strength, this theory accounts for the influence of crack propagation, energy release, and the development of the fracture process zone (FPZ) [4,5]. Furthermore, recent advancements in numerical modeling and experimental studies have refined Bažant's approach, incorporating fracture energy concepts and cohesive zone models to enhance predictive accuracy [6,7].

The theory was explained by expressing nominal strength (σ_N) as follows [4]:

$$\sigma_N = Bf_t^{'}\left(1+\frac{D}{D_0}\right)^{-\frac{1}{2}} \tag{1}$$

where f_t is the size-independent tensile strength of materials, D is the size of specimen, D_0 is a parameter based on structural geometry, and B is a dimensionless constant parameter indicating the solution according to plastic limit analysis based on the strength method. Both B and D_0 are based on the type of materials and geometry of specimens.

An effective-elastic crack model was developed to simulate the fracture behavior and size effect in quasi-brittle materials like concrete [5]. The size effect method (SEM) was introduced for a series of geometrically similar specimens of different sizes subjected to three-point bending (TPB) tests. This approach relies solely on the maximum applied load (P_{Max}) for each specimen [5].

The fracture parameters resulting from this method are independent of the specimen size. The size effect method (SEM) was investigated in accordance with RILEM TC-89 recommendations [6]. The parameters B and D_0 are experimental coefficients that depend on the material type and specimen geometry. These coefficients can be determined using regression analysis as follows:

$$y = Ax + C \tag{2}$$

$$\text{x=D, y=}\left(\frac{1}{\sigma_N}\right)^2,\ D_0 = \frac{C}{A}\ ,\ B = \frac{1}{\sqrt{C}} \tag{3}$$

in which A =slope and C = y-intercept of the regression line.

The following two equations were proposed in previous studies [8,10]:

$$G_f^B = \frac{\left(Bf_t^{'}\right)^2 D_0 g(\alpha_0)}{E'} \tag{4}$$

$$c_f = \frac{D_0 g(\alpha_0)}{g'(\alpha_0)} \tag{5}$$

where c_f = effective length of process zone

$$g(\alpha_0) = k^2(\alpha_0) \tag{6}$$

where $g(\alpha_0)$ is the non-dimensional energy release rate, and $g'(\alpha_0)$ is the derivative of with $g(\alpha_0)$ respect to the relative initial crack length $\alpha_0 = a_0/D$.

E and $E' = E/(1-\nu^2)$ are the Elastic modulus for plane stress and plane strain conditions respectively, with ν being Poisson's ratio.

The obtained fracture energy (G_f^B) is considered size-independent, as reported in previous studies [8].

For Notched beams in TPB test setup

$$k(\alpha_0) = \frac{p_{S/D}(\alpha_0)\sqrt{\alpha_0}}{(1+2\alpha_0)(1-\alpha_0)^{3/2}} \tag{7}$$

For function $p_{S/D}(\alpha_0)$, An interpolation formula applicable to any ratio of net span (S) to beam depth (D) was developed in previous studies [9,10]:

$$p_{S/D}(\alpha_0) = p_\infty(\alpha_0) + \left(\frac{4D}{S}\right)\left[p_4(\alpha_0) - p_\infty(\alpha_0)\right] \tag{8}$$

Function $p_\infty(\alpha_0)$ and $p_4(\alpha_0)$, which correspond to cases of pure bending and S/D=4, are

$$p_\infty(\alpha_0) = 1.989 - \alpha_0(1-\alpha_0) \times \left[0.448 - 0.458(1-\alpha_0) + 1.226(1-\alpha_0)^2\right] \tag{9}$$

$$p_4(\alpha_0) = 1.9 - \alpha_0\left[-0.089 + 0.603(1-\alpha_0)\right] - 0.441(1-\alpha_0)^2 + 1.223(1-\alpha_0)^3 \tag{10}$$

GEOMETRICAL PROPERTIES OF BEAMS

Tab.1 shows the geometrical properties of the beams adopted in the present study. The beams grouped as B series with five different sizes. In the nomenclature employed: B-SB75, the first letter B represent beam series, SB represents small beam and last digit represents depth or size of beam. The MB stands for medium beam, LB for large beam, VB for very large beam & HB for huge beam.

To save computational time and memory, the central part of the beam is modeled as a heterogeneous section with a fine mesh, while the side parts are modeled as homogeneous sections. This approach is illustrated in Fig.1-4. The heterogeneous section in the central part allows for a detailed representation of the microstructure where stress and strain concentrations are expected to be higher, whereas the homogeneous side sections reduce computational demands without significantly affecting the accuracy of the overall model. This method strikes a balance between accuracy and computational efficiency, ensuring that the key areas of interest are accurately simulated.

Beam ID	Depth of beam (D) mm	Breath of beam (b) mm	Length of the beam (L) mm	Span (S) mm	Central part of beam (S_0) mm	Notch to depth ratio $\alpha_0=a_0/D$	Depth of notch (a_0) mm	S/D
B-SB75	75	150	250	225	50	0.25	18.75	3
B-MB150	150	150	550	450	100		37.5	
B-LB250	250	150	1000	750	150		62.5	
B-VB500	500	150	2000	1500	300		125	
B-HB1000	1000	150	4000	3000	600		250	

Table 1: Geometrical properties of the beams.

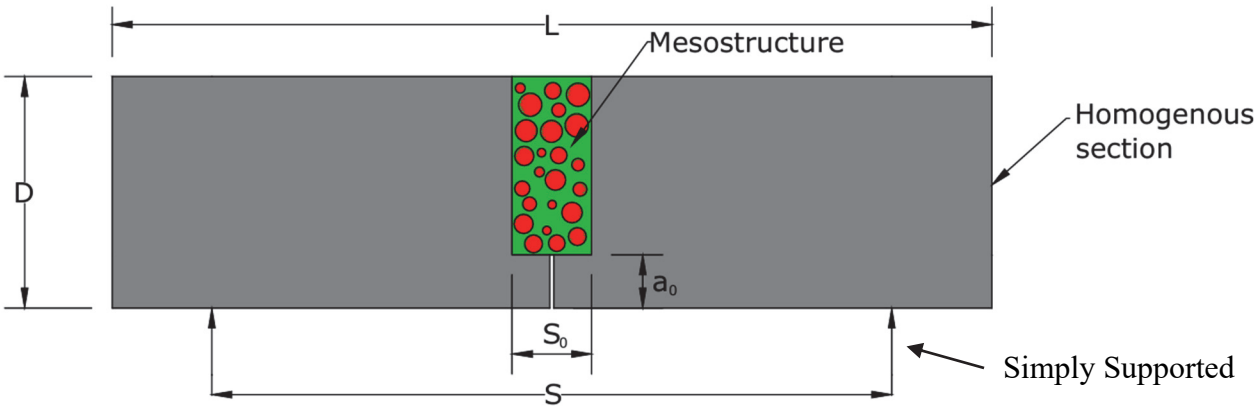

Figure 1: Spherical shape aggregates (SSA-Model).

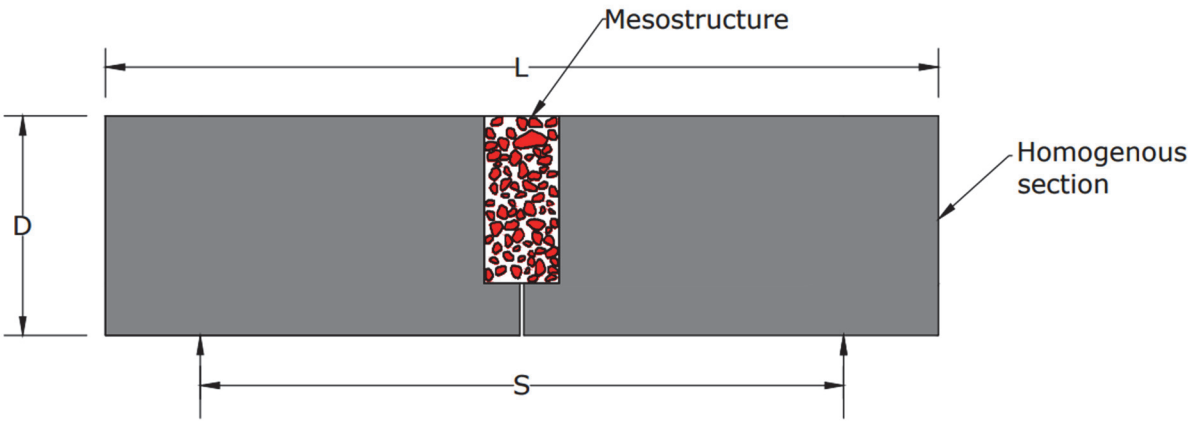

Figure 2: Realistic shape aggregates (RSA-Model).

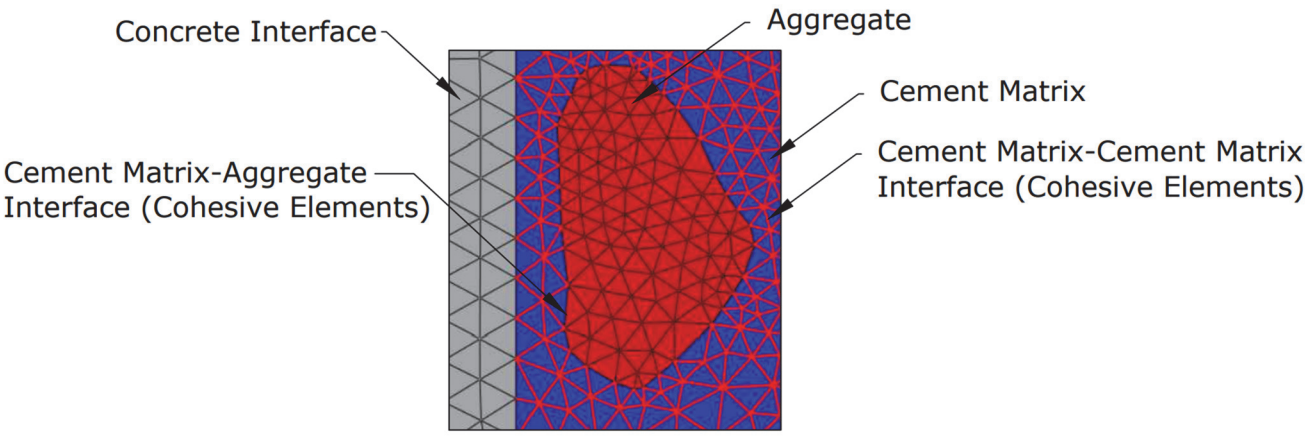

Figure 3: Interfaces in microstructure.

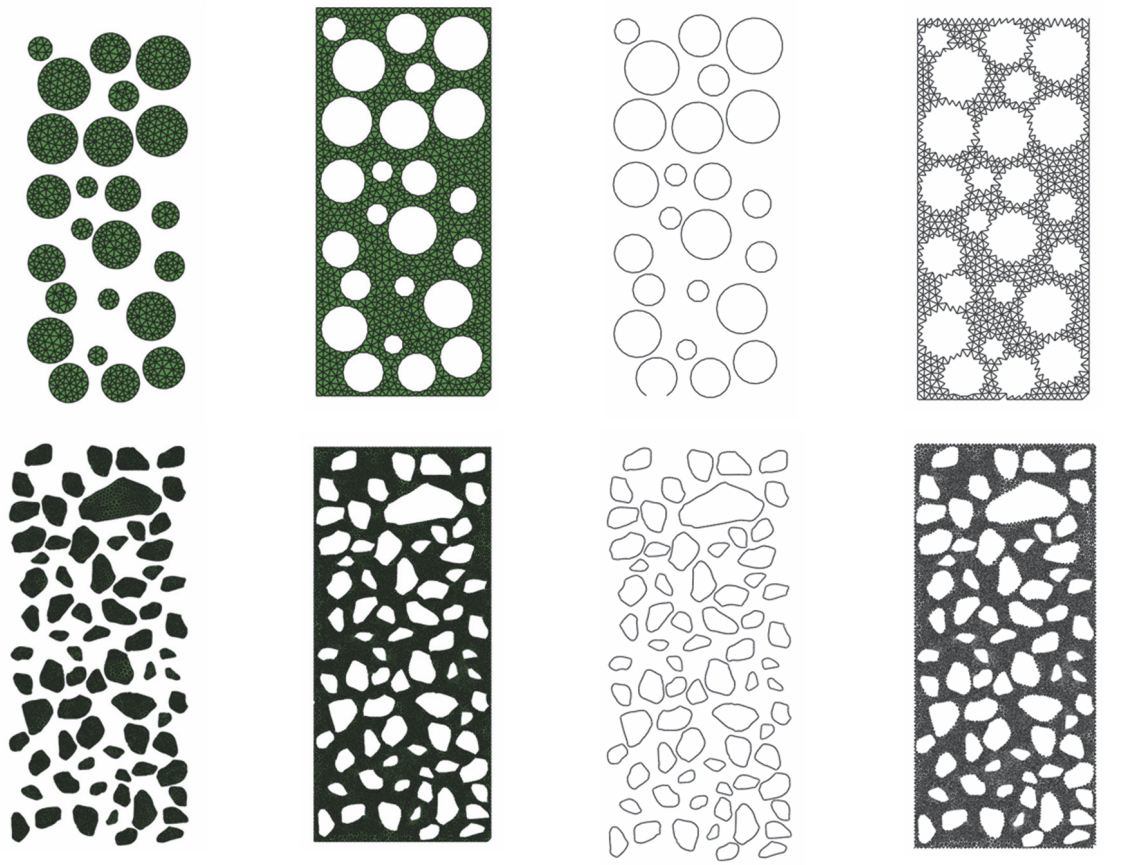

(a)Aggregates (b)Matrix © Cohesive elements at ITZ (d) Cohesive elements at Cement matrix

Figure 4: Heterogeneous region for SSA and RSA models.

MATERIAL PROPERTIES

In the FE model, the solid elements representing the mortar and aggregates are assumed to follow linear elastic behavior. Most of the deformation between adjacent solid elements is accommodated by the cohesive elements. The solid elements experience deformation only while the cohesive elements remain in their linear elastic range. Due to the extremely high initial stiffness of the cohesive elements, their deformation in this range is minimal, resulting in negligible deformation of the solid elements.

Elements	Parameter	Density (kg/m³)	Young's Modulus, E (MPa)	Poisson's ratio, υ	Traction-Separation Law		
					Elastic Stiffness (MPa)	Cohesive strength (MPa) (Damage initiation)	Fracture energy (N/mm)
Bulk	Aggregate	2800	47200	0.2	-	-	-
	Cement matrix	2400	29200	0.2	-	-	-
	Homogeneous beam part	2400	36100	0.2	-	-	-
Cohesive	CIEs	2400	-	-	10^6	3.5	0.168
	ITZs	2300	-	-	10^6	2.4	0.115

Table 2: Material properties adopted in FE analysis for concrete beam [11,12].

VALIDATION OF THE MODEL FOR DIFFERENT SHAPES OF AGGREGATES

In this study, spherical aggregates (appearing circular in 2D models) and realistically shaped aggregates were randomly distributed. The Monte Carlo method [13] was employed to generate and randomly place aggregates within the specimen's specified dimensions and aggregate fraction. A Python script was used, incorporating a loop with check-and-reject functions to ensure proper placement, while Abaqus/CAE was employed for the analysis. The boundary conditions provided to suit simply supported beam with central point load. A displacement load was applied, consisting of 10,000 load steps with a constant load increment. This loading procedure allowed for the crack to penetrate through the entire beam height, providing a detailed understanding of the fracture process in concrete. The details of model generation and the adopted process were based on the literature [14,15]. Each type of beam was tested in three iterations, with coarse aggregate (CA) distributed at different positions in each iteration while maintaining the required grading and fraction.
In essence, crack propagation and fracturing in concrete numerical simulations are intricately tied to mesh generation. For finite element simulations where the cohesive crack paths are not known in advance, rather fine levels of discretization must be used to reduce the dependence of the cohesive crack paths on the mesh size. However, reducing the element size leads to an increase in computational cost, so a balance between computational cost and accuracy must be established. To this end, a mesh convergence study is performed in this work in terms of the mean stress–strain curve and the final fracture crack paths to find an optimal mesh size.

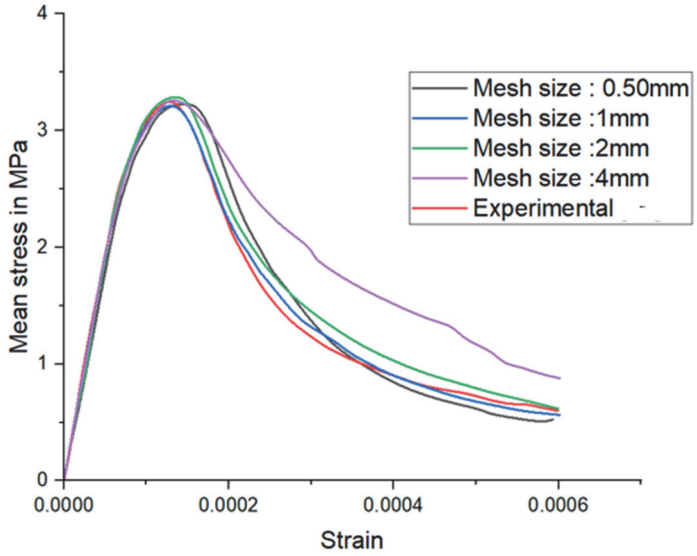

Figure 5: Mean stress–strain curve for a concrete sample shown in with different levels of discretization.

This study examined five different mesh sizes (0.5 mm, 1 mm, 2 mm, and 4 mm) [16]. The meshes finer than 1 mm resulted in poorly meshed regions, while coarser meshes caused element distortion and unfavourable mesh angles (Fig.5).

Considering that mesh sizes between 1 mm and 2 mm are widely employed in prior studies [16], this research adopted mesh sizes within this range based on a mesh sensitivity analysis.

The effect of shapes of aggregate particles investigated with beams of same geometry and material parameters with Spherical shape aggregates (SSA) and realistic shape aggregates (RSA). Fig. 6(i) presents the results for 10 beams with spherical aggregates, showing an average peak load of 7.10 kN whereas in Fig. 6(ii) average peak load of 7.85 kN noted for beams with irregular aggregates, which indicates that the spherical shaped aggregates load carrying capacity less compared to realistic shaped aggregates. Aggregates with angular shapes generate localized stress concentrations, which contribute to crack initiation and propagation. In contrast, spherical aggregates distribute stress more evenly, resulting in higher ultimate global beam strength and strain capacity. Comparable results have been documented in previous studies [2,4]. The maximum discrepancy of the peak load between the experimental and numerical values is 4.7 % for the mesostructure primarily composed of realistic shape aggregate and 6.5 % for the Spherical shape aggregates.

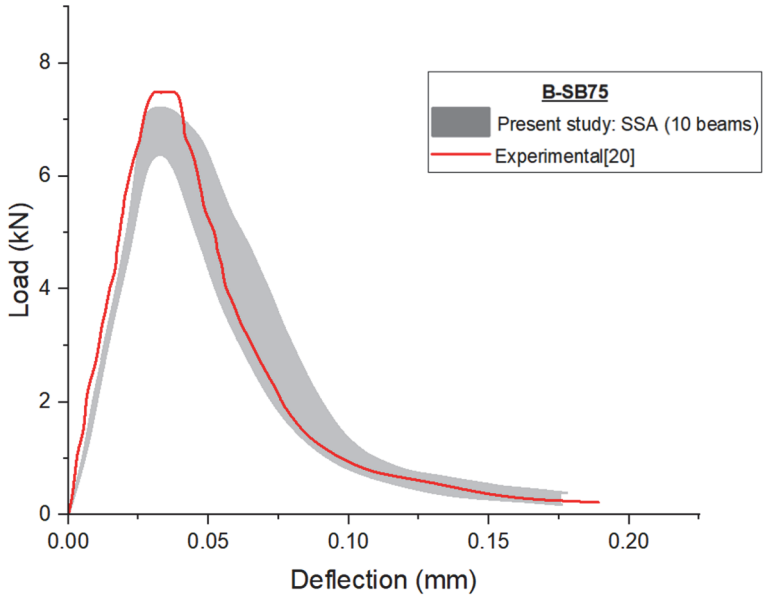

(i) Spherical shape aggregates (SSA model).

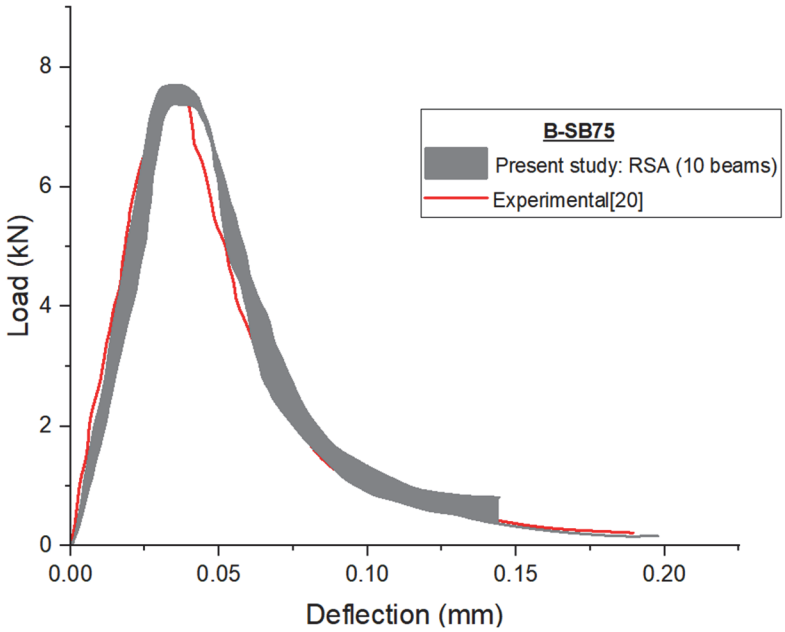

(ii) Realistic shape aggregates (RSA Model).

Figure 6: Load-deflection curves of 10 beams for validating present study.

From the final crack distribution and crack development process shown in Fig.6, it is evident that, under the influence of loading and boundary conditions, a macroscopic crack initiation zone forms in the lower-right area and propagates toward the loading point. In the spherical aggregate model, cracks begin to develop in the small aggregates and mortar and eventually reach aggregate (a), as shown in Fig. 7(i), where crack propagation is blocked and continues upward along the boundary of aggregate 'a'. This blocking effect is observed for aggregates 'b to f '.

In the realistic aggregate model, cracks initiate at the interface and in the mortar, and their development changes direction along the boundary of the aggregates based on the shape of the aggregate, as observed for aggregates 'a to g' , and h in Fig. 7(ii). Notably, in aggregate 'a', the crack direction shifts clearly, suggesting that the shape of the aggregate influences the direction of crack propagation. Therefore, it can be inferred that the shape of aggregates plays a role in crack propagation, with spherical aggregates mainly hindering crack growth, while realistic aggregates help guide it.

However, blocking effects are also evident in the realistic aggregate model, particularly for aggregate 'e' in Fig. 6(ii), when the aggregate's length direction is perpendicular to the fracture direction. Additionally, the softening section of the load-deflection curve for the realistic aggregate model gradually flattens, indicating that the geometric properties of aggregates exert both blocking and guiding effects on crack development.

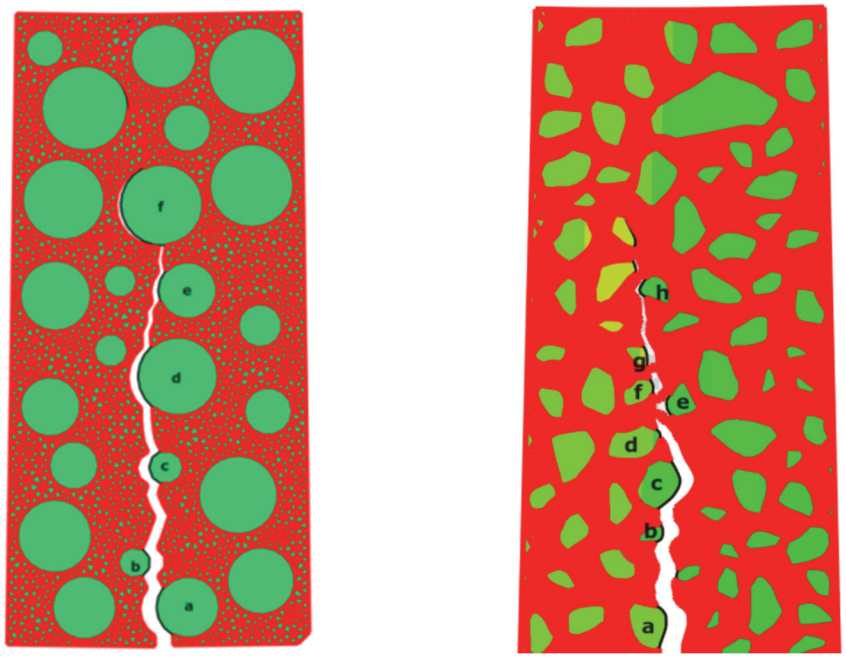

(i)SSA (ii)RSA

Figure 7: Crack Propogation under TPB test.

The results indicated that the geometric properties of aggregates have both blocking and guiding effects on crack development. The present study focuses on medium-strength concrete, where the crack propagation predominantly occurs along the weak ITZ (Refer Fig.7). However, in high-strength concrete, the ITZ is significantly strengthened due to the reduced porosity and improved bonding between the matrix and the aggregate. As a result, the crack is more likely to propagate through the aggregate itself, destroying it and altering its trajectory.

NUMBER OF ELEMENTS AND AVERAGE TIME TAKEN BY SSA AND RSA MODELS

The geometric properties of the beams for present study given in Tab.1. Fraction of aggregate considered 40% and M45 concrete adopted. The Tab.3 presents the number of elements and average time taken during analysis for each type of beam.

As per the Tab.3, number of elements increases with 1.95 to 3.52 times for RSA model due to more irregularity in the elements compared to SSA model. Time taken for analysis also 1.86 to 2.69 times SSA model, since more time required to obtain convergence in the analysis. Three iterations for each size carried out for analysis.

Beam ID	SSA		RSA		RSA/SSA	
	Number of elements	Average time (Seconds)	Number of elements	Average time (Seconds)	Number of elements	Average time
B-SB75	22,897	2,250	52,612	5,117	2.29	2.27
B-MB150	45,436	11,913	87,046	22,236	1.95	1.86
B-LB250	67,017	21,478	1,59,995	53,628	2.38	2.49
B-VB500	90,215	35,320	3,18,109	95,216	3.52	2.69
B-HB1000	1,27,012	72,516	-	-	-	-

Table 3: Number of elements and time taken for analysis for SSA and RSA models.

ANALYSIS OF LOAD-DEFLECTION AND LOAD-CMOD PLOTS

This study presents analysis of both SSA model and RSA model. The proposed numerical models predicted fracture behavior closely aligns with the average experimental results of a series of single-edge-notched beams (SENB) concrete specimens [20]. The cracking pattern is also more realistic than the conventional concrete material models. Fig.8 shows the typical cracks observed at failure.

Load versus deflection and Load versus CMOD plots obtained from the present study are compared to experimental results [20] with respect to different depths as shown in Fig.9-13. It is observed that compared to small size beams large size beams B-VB-500 and B-HB-1000 have not shown much softening and the failure behavior is closer to brittle. Although ther are marginal differences in the maximum central deflection.

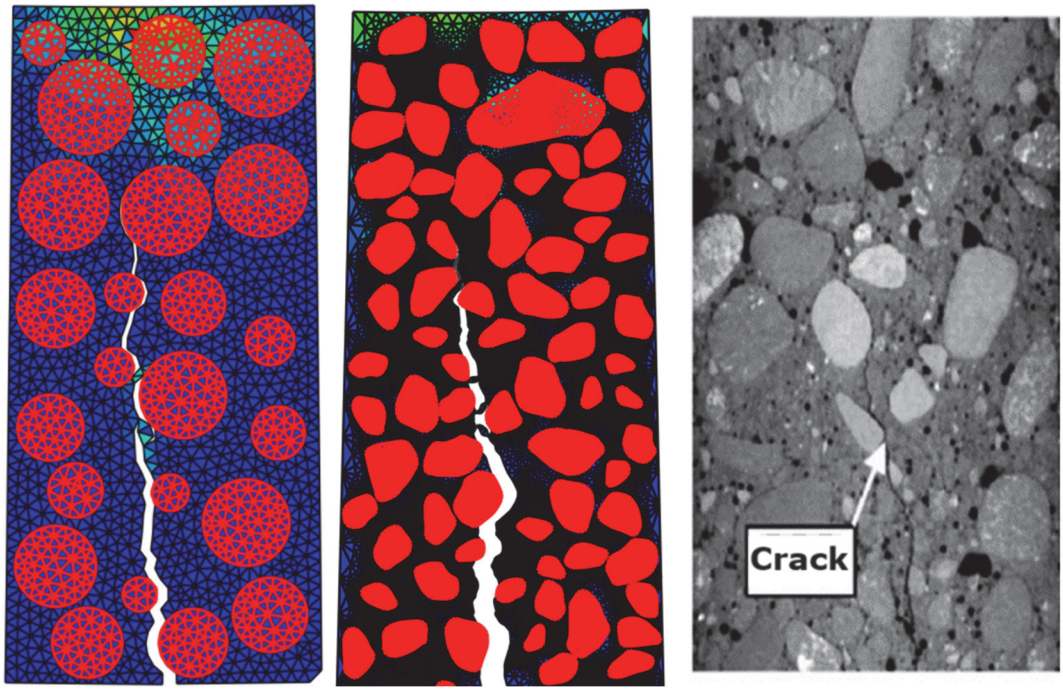

(i) Present study SSA and RSA Models (ii) Experimental

Figure 8: Typical cracks at failure of beams under TPB tests.

Tab.4 presents the P_{Max} for B-SB75, B-MB150, B-LB250, B-VB500 & B-HB1000 under TPB test. The study compares the results of SSA (spherical shaped aggregates) models and RSA (realistic shaped aggregates) models with experimental data [20]. Each beam depth has multiple trails to ensure repeatability and reliability of results. The percentage differences between the experimental results and the SSA and RSA models are calculated to evaluate the accuracy of the models. It is observed that maximum peak load (P_{Max}) of 6.9kN recorded for B-SB-75 whereas 49.4kN for B-HB-1000 for SSA beams. The percentage variation of P_{Max} ranges between 3.32% -8.69% in case of SSA model and 2.31% - 8.13% in case of RSA models.

Both SSA and RSA models show reasonably close agreement with the experimental results [20]. RSA models generally show slightly better agreement with experimental results than SSA models. The SSA models exhibit slightly higher standard deviations compared to the RSA models, suggesting greater variability in their results. Moreover, the RSA model shows a closer correlation with experimental data, particularly for smaller beam sizes.

Beam ID	Iteration	Present study				Experimental P_{Max} (kN)	SSA	RSA
		SSA		RSA				
		P_{Max} (kN)	μ, SD, μ±3*SD (99.7%)	P_{Max} (kN)	μ, SD, μ±3*SD (99.7%)		% Difference	% Difference
B-SB75	1	7.2	**6.90** 0.29 7.78, 6.02	7.5	**7.33** 0.12 7.71, 6.96	7.50	8.69	2.31
	2	6.5		7.2				
	3	7.0		7.3				
B-MB150	1	12.7	**12.63** 0.74 14.84, 10.42	13.1	**12.73** 0.26 13.52, 11.95	13.05	3.32	2.51
	2	13.5		12.5				
	3	11.7		12.6				
B-LB250	1	17.1	**18.10** 0.78 20.44, 15.76	17.4	**18.00** 0.43 19.30, 16.70	18.85	4.14	4.72
	2	18.2		18.4				
	3	19.0		18.2				
B-VB500	1	29.1	**30.33** 0.98 33.28, 27.39	30.2	**30.24** 0.56 31.23, 27.90	32.70	7.81	8.13
	2	31.5		30.1				
	3	30.4		29.8				
B-HB1000	1	50.2	**49.40** 0.59 51.17, 47.63	-		52.23	5.72	
	2	49.2		-				
	3	48.8		-				

Table 4: Peak load (kN/m) under TPB tests.

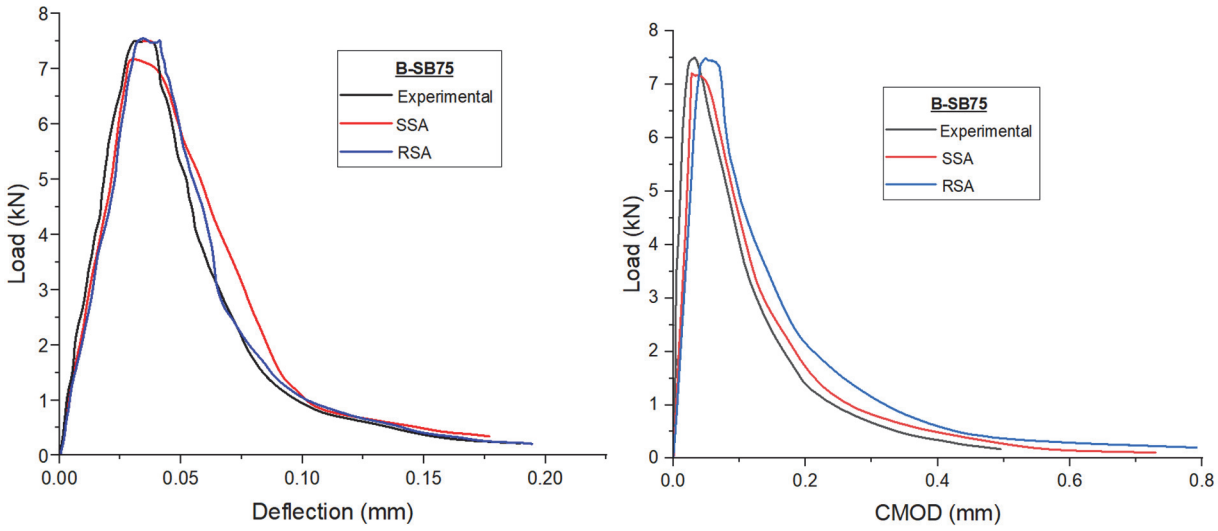

Figure 9: Load deflection & CMOD curves for B-SB75.

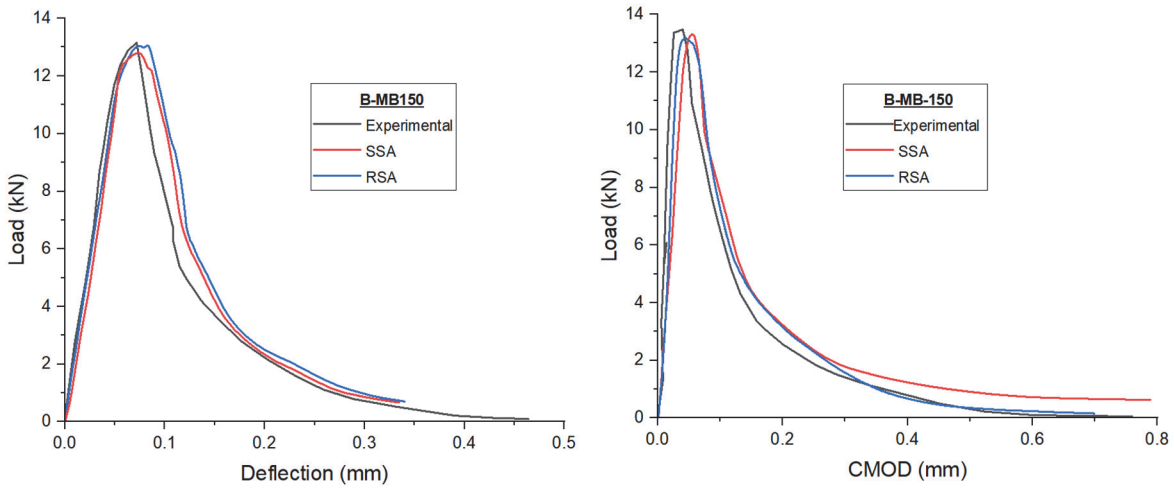

Figure 10: Load deflection & CMOD curves for B-MB150.

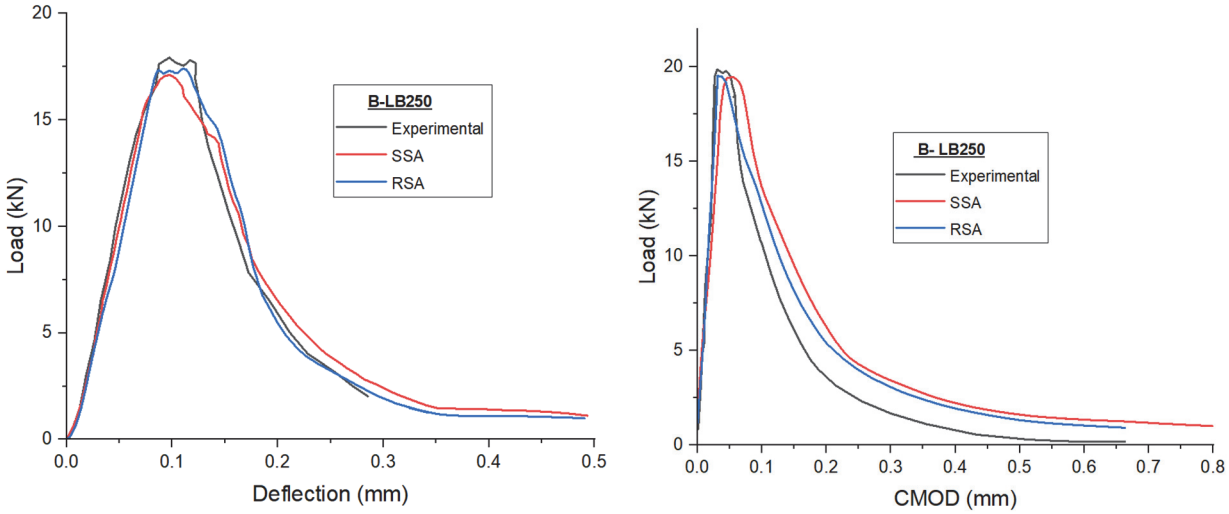

Figure 11: Load deflection & CMOD curves for B-LB250.

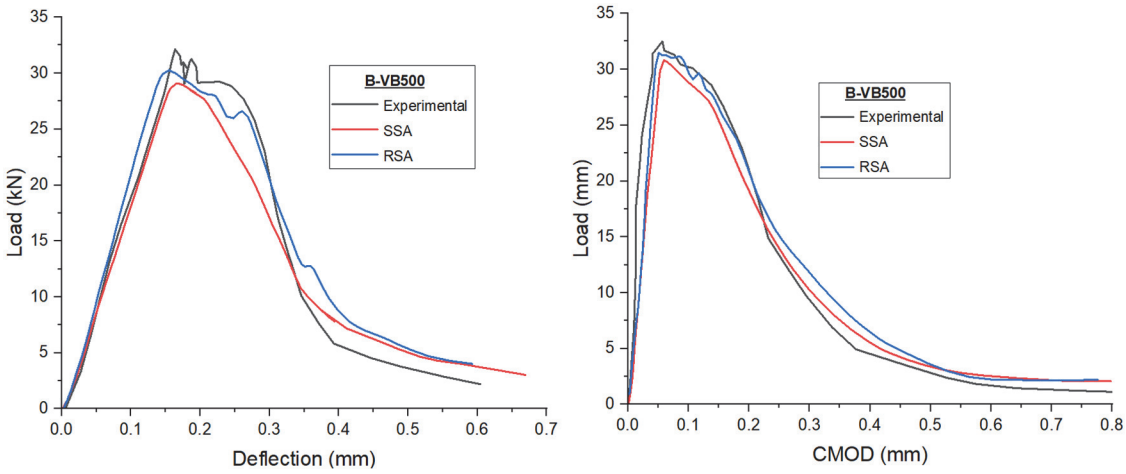

Figure 12: Load deflection & CMOD curves for B-VB500.

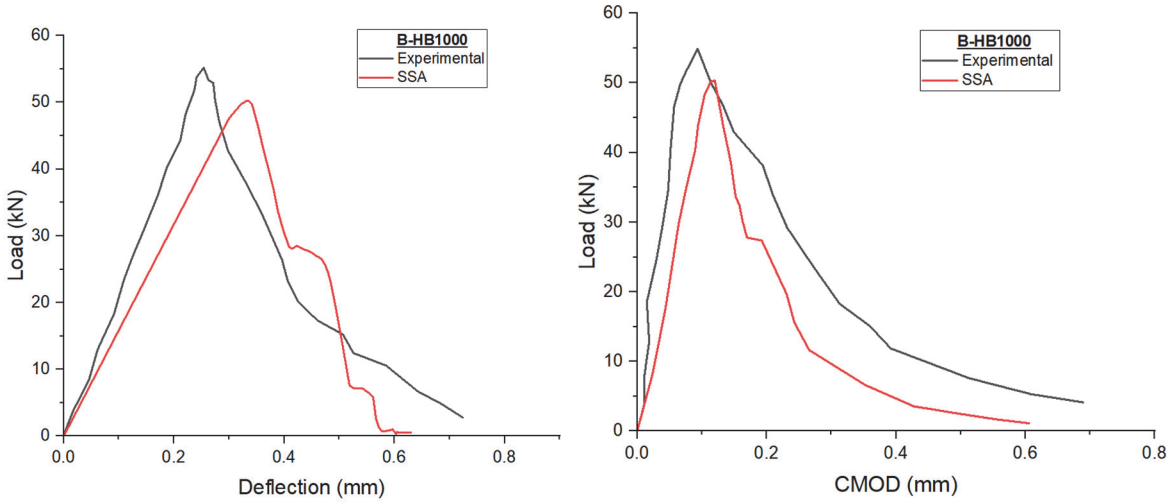

Figure 13: Load deflection & CMOD curves for B-HB1000.

EVALUATION OF SIZE DEPENDENT FRACTURE ENERGY (WORK-OF-FRACTURE METHOD)

Tab.5 presents the fracture energy (G_f) for B-SB75, B-MB150, B-LB250, B-VB500 & B-HB1000 adopting work of fracture method [9]. This study compares the results of SSA (spherical-shaped aggregate) models and RSA (realistic-shaped aggregate) models with experimental data [20].

It is observed that G_f tends to increase with the depth of the specimen, although the values seemed to plateau (Fig.14) for the two largest sizes. Previous studies [17–21] have also observed an increasing trend in G_f with D. It has been suggested that this rise in fracture energy with size may be partially due to the corresponding increase in applied load.

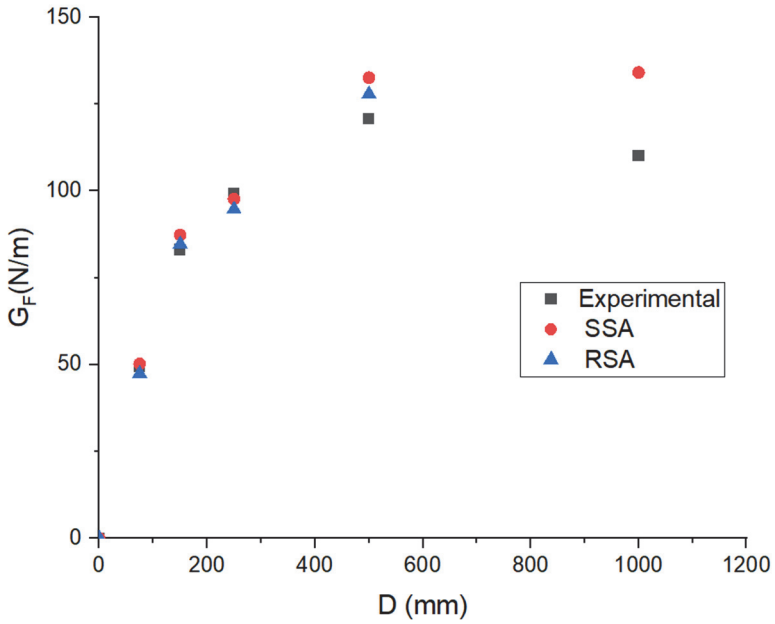

Figure 14: Average G_f versus depth of beam.

Beam ID	Iteration	Present study				Experimental	SSA	RSA
		SSA		RSA				
		G_f (N/m)	μ, SD, μ±3*SD (99.7%)	G_f (N/m)	μ, SD, μ±3*SD (99.7%)	G_f (N/m)	% Difference	% Difference
B-SB75	1	50.35	**50.17** 2.51 57.71, 42.62	48.57	**47.41** 3.46 57.79, 37.03	49.3	1.74	3.98
	2	47.00		48.15				
	3	53.15		51.23				
B-MB150	1	83.34	**87.32** 2.89 96.00,78.65	88.63	**84.66** 2.13 91.05, 78.28	83.1	4.82	6.23
	2	90.12		86.42				
	3	88.51		85.90				
B-LB250	1	92.33	**90.34** 1.77 95.66, 85.02	88.98	**94.70** 6.08 112.94, 76.46	99.2	9.80	4.75
	2	88.02		103.12				
	3	90.67		92.00				
B-VB500	1	146	**127.92** 13.06 167.09, 88.75	149	**127.89** 15.92 175.66, 80.12	120.8	5.56	5.54
	2	122.15		124.12				
	3	115.62		110.55				
B-HB1000	1	149	**134.14** 10.57 165.84, 102.44	-		110.1	17.96	
	2	125.32		-				
	3	128.11		-				

Table 5: Fracture energy (G_f) from work -of-fracture method under TPB test.

The G_f obtained in this study ranges from 50.17 N/m to 134.14 N/m for SSA specimens and from 47.41 N/m to 127.89 N/m for RSA specimens. An increase in beam depth corresponds to a rise in G_f, highlighting its dependence on specimen dimensions. A comparison with experimental data for various beam depths revealed a variation of approximately 3%. The G_f values from this study closely align with experimental results [20], with a low coefficient of variation (CoV), indicating consistency in the findings.

LINEAR REGRESSION FOR RSA AND SSA BEAMS

Bazant et al. [22] have indicated that fracture energy obtained from a large specimen is not beset with size effects. Also, while using the SEL, they have recommended a good range of beam depths so that the results from the regression analysis are reliable and acceptable.

The peak load obtained from notched beams in the TPB test is essential for calculating key fracture parameters, including initial fracture energy, fracture process zone length, and the stress intensity factor in SEM. Fig.16 illustrates the relationship between nominal flexural strength (σ_Z) and beam size(D). A fitting curve for the experimental results is generated using the linear regression method, as shown in the figure. The results from the present study are also included and compared with the experimental data, showing a strong agreement, as evidenced by the close alignment of the present results with the fitting curve.

The Fig.15(a) and Fig.15(b) illustrates the linear regression results of SSA and RSA respectively, in which the line slope of $A = 3.497 \times 10^{-4}$ and y-intercept of C = 0.113 was obtained with the correlation coefficient of $R^2 = 0.992$ for SSA while $A = 4.575 \times 10^{-4}$, C=0.080 and $R^2 = 0.95$ in which D=1000 not considered for analysis.

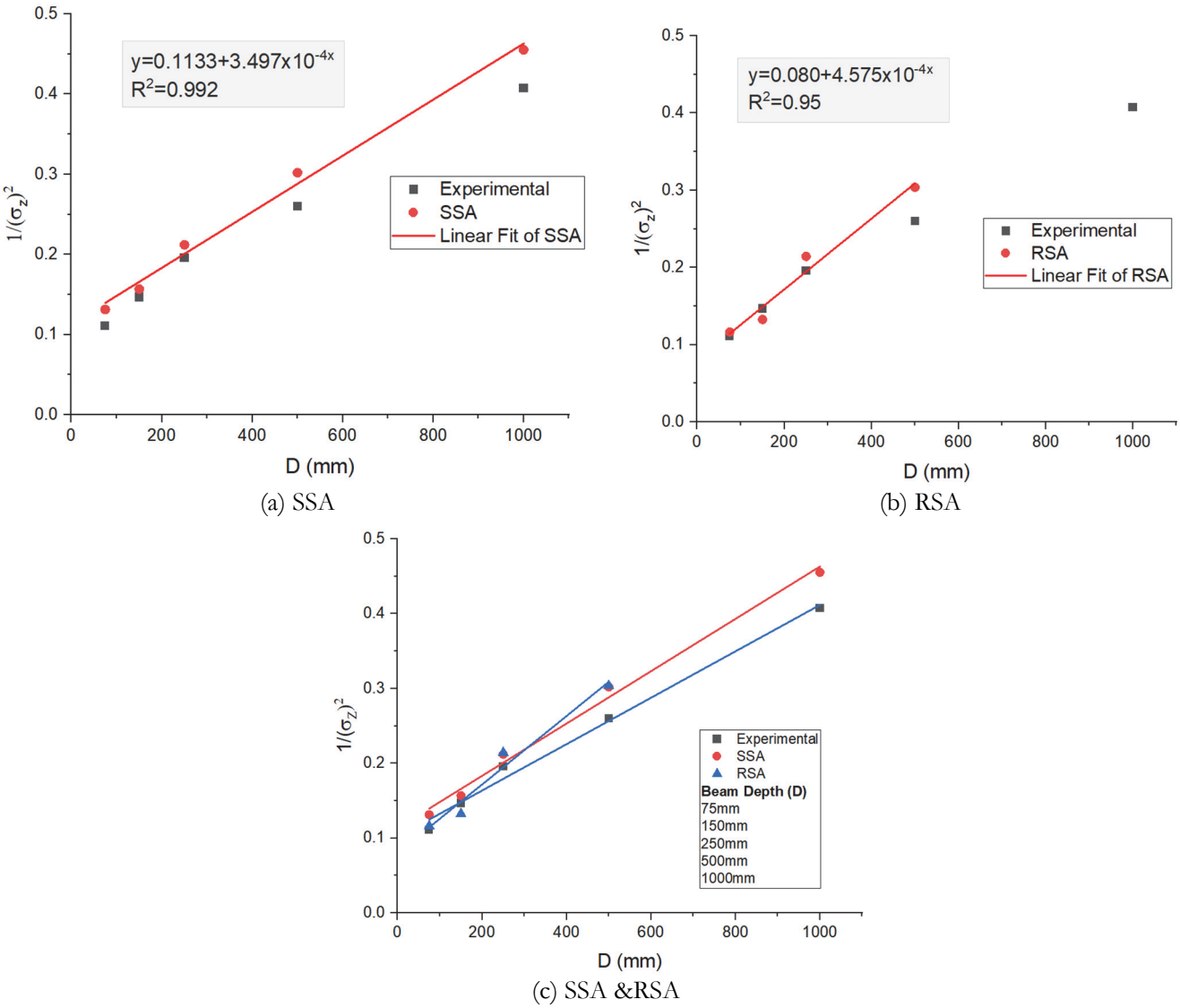

(a) SSA (b) RSA

(c) SSA &RSA

Figure 15: Linear Regression plot for RSA and SSA beams.

SIZE EFFECT PARAMETERS

Using Eqns. 1-10, the size effect parameters and fracture properties obtained from the size effect analysis are presented in Tab.6. These predicted fracture parameters are compared with the experimental results, where both fracture energy and effective length are found to be qualitatively close to the experimental observations.

Using the parameters from Tab.7 obtained in the present study, a plot of $\log(\sigma_N/B_f)$ versus $\log(D/D_0)$ is created and compared with Bažant's size effect curve for SSA, RSA, and the combined SSA & RSA models, along with the experimental results (Ref. Fig.16)

The plots reveal that the curve initially follows a nearly horizontal trend, indicating the absence of a size effect. As the curve progresses, it transitions into a straight line with a slope of approximately -1/2, approaching the Linear Elastic Fracture Mechanics (LEFM) zone. In between, there is a smooth, curved transitional region. Therefore, it can be concluded that all plots exhibit a size effect, consistent with Bažant's size effect law.

Fig.16 presents Bažant's size effect curve fitted to the experimental data [20] for both SSA and RSA specimens. According to this curve, ductile concrete aligns more closely with the strength criterion, whereas brittle concrete follows the LEFM behavior. Fig.17 further illustrates that smaller specimen (75mm, 150mm, and 250mm) exhibit behavior closer to the strength criterion, while larger specimens (500mm and 1000mm) approach the LEFM behavior. This indicates that smaller

specimens show ductile characteristics, whereas larger specimens display more brittle behavior. Consequently, LEFM is better suited for designing larger specimens, while the strength criterion is more appropriate for smaller ones.

Parameter	Experimental	For all beam Present study		For beam size 250mm, 500mm and 1000mm Experimental	Present study	
		SSA	RSA		SSA	RSA
k_0	0.877	0.877	0.877	0.877	0.877	0.877
k'_0	2.274	2.274	2.274	2.274	2.274	2.274
D_0 (mm)	283.1	323.2	324.1	466.3	425	-
Bf_t (MPa)	3.16	2.97	3.54	3.00	2.72	-
c_f (mm	54.6	62.32	62.59	89.9	82.0	-
G_f^B (N/m)	59.2	62.66	62.73	73.8	69.0	-

Table 6: Size effect parameters and fracture properties from size effect analysis.

Beam ID	D (mm)	P_{Max} (kN)	σ_N (Mpa)	$\frac{1}{(\sigma_N)^2}$	C	A	Bf_t	D_0
			SSA model					
B-SB75	75	6.9	2.76	0.1313				
B-MB150	150	12.63	2.526	0.1567				
B-LB250	250	18.1	2.172	0.2120				323
B-VB500	500	30.33	1.8198	0.3020	0.113	0.00035	2.97	
B-HB1000	1000	49.4	1.482	0.4553				
			RSA model					
B-SB75	75	7.33	2.932	0.1163				
B-MB150	150	13.73	2.746	0.1326				
B-LB250	250	18	2.16	0.2143				237
B-VB500	500	30.24	1.8144	0.3038	0.090	0.00038	3.33	

Table 7: Parameters for bi-logarithmic plotting (Fig. 16).

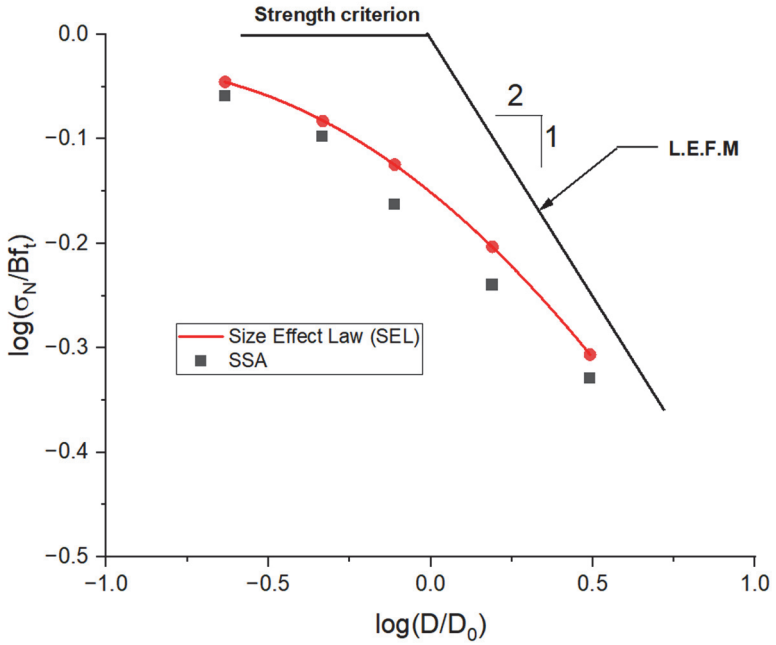

(a) SSA

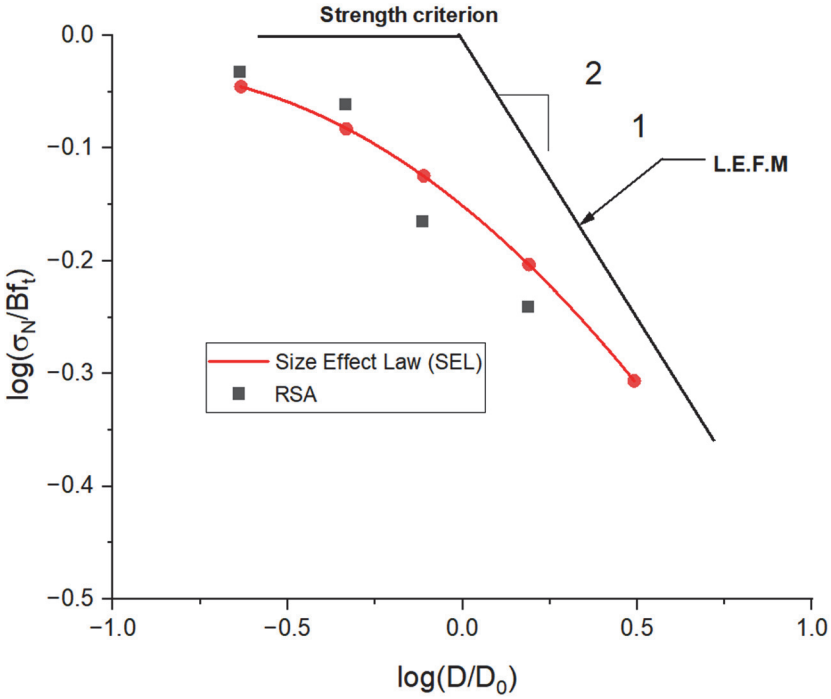

(b) RSA

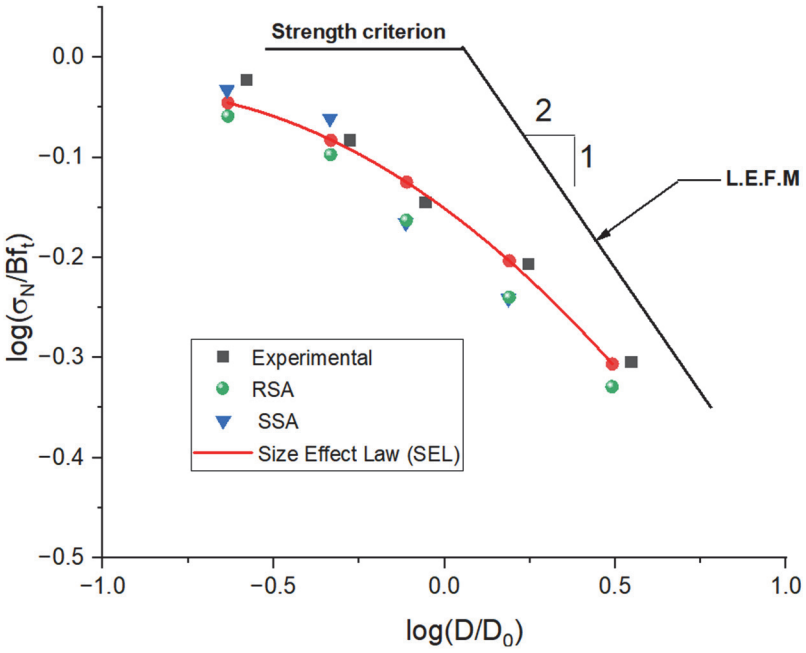

(c) SSA & RSA

Figure 16: Size effect law curves for RSA and SSA beams.

Additionally, it is evident from Fig.17 that the modeling approach employed in this study effectively captures the size effect phenomenon. As anticipated, for larger specimens, the nominal strength is governed by LEFM, whereas for smaller specimens, the nominal strength asymptotically approaches the plastic limit.

The findings of this study closely align with Bažant's size effect law (BSL), demonstrating that BSL effectively characterizes the size effect on the flexural strength of concrete beams. The strong correlation between the study's data and the theoretical BSL curve, derived from experimental results, further reinforces the reliability of this approach.

Both experimental and numerical results indicate that nominal flexural strength decreases as beam depth increases from 75mm to 1000mm. The BSL accurately describes this size-dependent behavior in concrete beams. Finally, the present study's results are well-validated through their strong agreement with experimental data [20].
The findings of this study closely align with Bažant's Size Effect Law (BSL), demonstrating that BSL effectively characterizes the size effect on the flexural strength of concrete beams. The strong correlation between the study's numerical and experimental data with the theoretical BSL curve reinforces the reliability of this approach.
Both experimental and numerical results indicate that nominal flexural strength decreases as the beam depth increases from 75 mm to 1000 mm, highlighting the inherent size-dependent behavior of concrete fracture. This is consistent with the observations made in other numerical investigations, where fracture processes in concrete have been successfully captured using advanced modeling techniques [23] showing that fracture energy dissipation increases with specimen size, in agreement with BSL predictions. The transition from ductile to brittle failure mechanisms is accurately represented by BSL when considering meso-scale heterogeneity in concrete [24]. Findings reinforce the need to incorporate non-linear fracture mechanics for large-scale concrete structures, aligning with the present study's results. Furthermore, [25] size-dependent cracking patterns in three-point bending beams and confirmed that fracture process zone (FPZ) development scales with beam depth, affecting nominal flexural strength which match the decreasing strength trends observed in the current study. The present study's findings are thus well-validated, demonstrating a strong agreement with experimental data and further confirming that BSL remains a robust tool for predicting the size effect in concrete beams.

CONCLUSIONS

The size effect analysis of the present results was performed and compared with both experimental findings and Bažant's size effect law, revealing key insights into fracture behavior in notched concrete beams.

1. The numerical model effectively captures the experimental response for notched specimens, particularly in terms of strength and post-peak behavior. However, minor discrepancies were observed in the post-peak regions, with 3.32% to 8.69% variation in the SSA model and 2.31% to 8.13% in the RSA models.
2. The average fracture energy (G_f), determined using the work-of-fracture method, increases with size and tends to stabilize asymptotically as the beam size increases.
3. The G_f values for SSA models range from 50.17 to 127.92 kN/m, while those for RSA models vary from 47.41 to 127.89 kN/m, closely matching the experimental range of 49.3 to 120.8 kN/m. It was observed that for smaller beam depths, RSA models showed closer agreement with experimental results.
4. The present study, along with experimental size-effect data from the literature, exhibits the expected size-dependent behavior. Fitting the data to Bažant's size effect law confirmed a close correlation.
5. Both numerical and experimental results indicate a decreasing trend in nominal strength as beam depth increases from 75 mm to 1000 mm, aligning well with Bažant's size effect law for predicting the size-dependent flexural strength of concrete beams.

While this study provides significant findings, several areas require further investigation:

- Consideration of aggregate texture and morphology to better replicate real concrete heterogeneity in large-size beams using numerical models.
- Extending the study to large-scale structural elements, such as bridges and slabs, to assess the practical implications of size effect in real-world concrete structures.

By addressing these areas, future research can enhance the accuracy, applicability, and computational efficiency of fracture modeling, contributing to improved predictive capabilities for concrete structures.

REFERENCES

[1] Picazo, Á., Alberti, M. G., Gálvez, J. C., Enfedaque, A. and Vega, A. C. (2019). The size effect on flexural fracture of polyolefin fibre-reinforced concrete. Applied Sciences, 9(9), 1762. DOI: 10.3390/app9091762.
[2] Bažant, Z. P. Planas, J. (1998). Fracture and Size Effect in Concrete and Other Quasi-Brittle Materials. CRC Press. ISBN 9780849382840.
[3] Bažant, Z. P., Ozbolt, J. and Eligehausen, R. (1994). Fracture size effect: Review of evidence for concrete structures. Journal of Structural Engineering, 120(8), pp. 2377-2398.

[4] Bažant, Z. P. (1998). Size effect in tensile and compression fracture of concrete structures: Computational modeling and design. In Fracture Mechanics of Concrete Structures, 3, pp. 1905–1922.
[5] Bažant, Z. P. and Kazemi, M. T. (1990). Determination of fracture energy, process zone length and brittleness number from size effect, with application to rock and concrete. International Journal of Fracture, 44, pp. 111-131.
[6] RILEM FMT 89. (1990). Size-effect method for determining fracture energy and process zone size of concrete. Materials and Structures, 23(6), pp. 461-465.
[7] Bažant, Z. P. and Planas, J. (1998). Fracture and Size Effect in Concrete and Other Quasibrittle Materials. Boca Raton, FL: CRC Press.
[8] Elices, M., Guinea, G. V. and Planas, J. (1992). Measurement of the fracture energy using three-point bend tests: Part 3 - Influence of cutting the P−δ tail. Materials and Structures, 25, pp. 327-334.
[9] Guinea, G. V., Planas, J. and Elices, M. (1998). Measurement of the fracture energy using three-point bend tests: Part 1 - Influence of experimental procedures. Materials and Structures, 31(4), pp. 231-237. DOI: 10.1007/BF02480471.
[10] Pastor, J., Guinea, G. V., Planas, J. and Elices, M. (1995). A new expression for the stress intensity factor for the three-point bending test specimen. Anales de Mecánica de la Fractura, 12, pp. 85-90.
[11] Trawiński, W., Tejchman, J. and Bobiński, J. (2018). A three-dimensional meso-scale modeling of concrete fracture, based on cohesive elements and X-ray CT images. Engineering Fracture Mechanics, 189, pp. 27-50. DOI: 10.1016/j.engfracmech.2017.10.003.
[12] Chen, H., Xu, B., Wang, J., Nie, X. and Mo, Y. L. (2020). XFEM-based multiscale simulation on monotonic and hysteretic behavior of reinforced-concrete columns. Applied Sciences, 10(21), pp. 1-21. DOI: 10.3390/app10217899.
[13] Wang, X., Yang, Z. and Jivkov, A. P. (2015). Monte Carlo simulations of mesoscale fracture of concrete with random aggregates and pores: A size effect study. Construction and Building Materials, 80, pp. 262-272. DOI: 10.1016/j.conbuildmat.2015.02.002.
[14] Vishwanatha, H. S., Muralidhara, S. and Raghu Prasad, B. K. (2023). Fracture Simulation of Concrete Beams to assess softening behavior by varying different fractions of Aggregates. Fracture and Structural Integrity, 18(67), pp. 43–57. DOI: 10.3221/IGF-ESIS.67.04.
[15] Vishwanatha, H. S., Muralidhara, S. and Raghu Prasad, B. K. (2025). Investigation on the characterization and modelling of Fracture Process Zone behavior in Concrete Beams subjected to Three-Point Loading Tests. Fracture and Structural Integrity, 19(72), pp. 80–101. DOI: 10.3221/IGF-ESIS.72.07.
[16] Ren, X., Yang, W., Zhou, Y. and Li, J. (2008). Behavior of high-performance concrete under uniaxial and biaxial loading. ACI Materials Journal, 105(6), 548.
[17] Cooper, T. P. (2000). Size effects (macro-and micro-scale) on the fracture behavior of high strength concrete (Master's thesis). Department of Civil Engineering, Case Western Reserve University.
[18] Ozbolt, J. and Eligehausen, R. (2002). Size effect in concrete and reinforced concrete structures. In A. Carpinteri (Ed.), Proceedings of the International Union of Theoretical and Applied Mechanics (IUTAM) Symposium on Size-Scale Effects in the Failure Mechanisms of Materials and Structures (p. 290). London: Taylor and Francis.
[19] Elices, M. and Planas, G. (2002). Prediction of size-effect based on cohesive crack models. In A. Carpinteri (Ed.), Proceedings of the International Union of Theoretical and Applied Mechanics (IUTAM) Symposium on Size-Scale Effects in the Failure Mechanisms of Materials and Structures (p. 309). London: Taylor and Francis.
[20] Ameli, Z., Rahman, M. M. and Carloni, C. (2023). Largest Experimental Investigation on Size Effect of Concrete Notched Beams. Journal of Engineering Mechanics. 150. DOI: 10.1061/JENMDT.EMENG-7225.
[21] Carloni, C., Santandrea, M. and Baietti, G. (2019). Influence of the width of the specimen on the fracture response of concrete notched beams. Engineering Fracture Mechanics, 216, 106465. DOI: 10.1016/j.engfracmech.2019.04.039.
[22] Bazant, Z. P. and Pfeiffer, P. A. (1987). Determination of Fracture Energy From Size Effect and Brittleness Number. ACI Materials Journal, 84(6), pp. 463–480. DOI: 10.14359/2526.
[23] El-Tohfa, A. and Mukhtar, F. (2023). Fracture and size effect analysis in concrete using 3-D G/XFEM and a CZM-LEFM correlation model: Validation with experiments. Computers and Structures, 282, 107043. DOI: 10.1016/j.compstruc.2023.107043.
[24] Huang, Y.J., Yang, Z.J., Liu, G.H. and Chen, X.W. (2016). An efficient FE–SBFE coupled method for mesoscale cohesive fracture modelling of concrete. Computational Mechanics, 58(4), pp. 635 – 655. DOI: 10.1007/s00466-016-1309-8.
[25] Wang, Z., Zhang, W. and Huang, Y. (2023). Experimental and Numerical Study of Concrete Fracture Behavior with Multiple Cracks Based on the Meso-Model. Materials, 16(18), 6311.